Earth and Planetary Science Letters 567 (2021) 117013

Contents lists available at ScienceDirect

Earth and Planetary Science Letters

www.elsevier.com/locate/epsl

Timescales of impact melt sheet crystallization and the precise age of the Morokweng impact structure, South Africa

Gavin G. Kenny [a,b,*], Claire O. Harrigan [b], Mark D. Schmitz [b], James L. Crowley [b], Corey J. Wall [b], Marco A.G. Andreoli [c], Roger L. Gibson [c], Wolfgang D. Maier [d]

[a] Department of Geosciences, Swedish Museum of Natural History, SE-104 05 Stockholm, Sweden
[b] Isotope Geology Laboratory, Department of Geosciences, Boise State University, 1910 University Drive, Boise, ID 83725, USA
[c] School of Geosciences, University of the Witwatersrand (WITS), Johannesburg, South Africa
[d] School of Earth and Ocean Sciences, Cardiff University, Park Place, Cardiff CF10 3AT, UK

ARTICLE INFO

Article history:
Received 18 January 2021
Received in revised form 11 May 2021
Accepted 15 May 2021
Available online 25 May 2021
Editor: W.B. McKinnon

Keywords:
impact melting
zircon
baddeleyite
high-precision geochronology
thermal modeling
Jurassic–Cretaceous boundary

ABSTRACT

Impact cratering was a fundamental geological process in the early Solar System and, thus, constraining the timescales over which large impact structures cool is critical to understanding the thermal evolution and habitability of early planetary crusts. Additionally, impacts can induce mass extinctions and establishing the precise timing of the largest impacts on Earth can shed light on their role in such events. Here we report a high-precision zircon U–Pb geochronology study of the Morokweng impact structure, South Africa, which appears to have a maximum present-day diameter of ~80 km. Our work provides (i) constraints on the cooling of large impact melt sheets, and (ii) a high-precision age for one of Earth's largest impact events, previously proposed to have overlapped the *ca.* 145 Ma Jurassic–Cretaceous (J–K) boundary. High-precision U–Pb geochronology was performed on unshocked, melt-grown zircon from five samples from a borehole through approximately 800 m of preserved impact melt rock. Weighted mean $^{206}Pb/^{238}U$ dates for the upper four samples are indistinguishable, with relative uncertainties (internal errors) of better than 20 ka, whereas the lowermost sample is distinguishably younger than the others. Thermal modeling suggests that the four indistinguishable dates are consistent with *in situ* conductive cooling of melt at this location within 30 kyr of the impact. The younger date from the lowest sample cannot be explained by *in situ* conductive cooling in line with the overlying samples, but the date is within the ~65 kyr timeframe for melt-present conditions in footwall rocks below the impact melt sheet that is indicated by our thermal model. The Morokweng impact event is here constrained to 146.06 ± 0.16 Ma (2σ; full external uncertainty), which precedes current estimates of the age of the J–K boundary by several million years.

1. Introduction

Impact cratering has been a fundamental geological process controlling the evolution of planetary crusts in the inner Solar System. Given that early planetary crusts were widely reprocessed by impacts through mixing and burial by impact-generated melt (e.g., Marchi et al., 2014), understanding the rates at which large impact structures cool is critical to understanding the thermal evolution of these crusts, as well as the timescales over which impacts may have sterilized the near- and sub-surface (e.g., Abramov and Mojzsis, 2009) or provided habitats suitable for the development of life (e.g., Osinski et al., 2020).

Large impact events can also play a role in the evolution of life on Earth by triggering extinction events. To date, the Chicxulub impact event, which produced an ~180-km-diameter impact structure in the Yucatán Peninsula, Mexico, and contemporaneous 66 Ma K–Pg mass extinction is the only established causal relationship between an impact and mass extinction (e.g., Schulte et al., 2010) but the possibility remains that other large impacts may have triggered mass extinctions. Accurate and precise radioisotopic dating of large impact structures can contribute to our understanding of the impact–mass extinction cause–effect relationship by (i) definitively ruling out correlation, and thereby causation, with extinction events, (ii) indicating a possible temporal overlap with an extinction event that can be investigated further, or (iii) defining which sedimentary successions may host a record of impact and its possible effects on the biosphere.

* Corresponding author.
E-mail address: gkennyeire@gmail.com (G.G. Kenny).

https://doi.org/10.1016/j.epsl.2021.117013

Here we apply high-precision zircon U–Pb geochronology and thermal modeling to an impact-generated melt sheet at one of the largest terrestrial impact structures, the Morokweng structure of South Africa, to (i) provide constraints on the rates at which impact structures cool, and (ii) determine a high-precision age for an impact event long considered to overlap with the *ca*. 145 Ma Jurassic–Cretaceous (J–K) boundary.

Numerical modeling has previously shed light on the timescales over which impact structures cool. A number of studies have modeled conductive cooling of impact craters (e.g., Ivanov, 2004, 2005; Onorato et al., 1978; Prevec and Cawthorn, 2002) with more recent work also incorporating the effects of convective cooling in structures that hosted impact-related hydrothermal systems (e.g., Abramov and Kring, 2004, 2007). The latter models suggest that melt sheets at two of the largest terrestrial impact structures (the ~180 km-diameter Sudbury impact structure in Canada, and the Chicxulub impact structure) had fully crystallized within 200 kyr of the impact event and the structures may have hosted active hydrothermal systems for up to 2.3 Myr after impact (Abramov and Kring, 2004, 2007). The hydrothermal mineral assemblage preserved in the peak ring of the Chicxulub structure supports this approximate timeframe while possibly indicating an even longer timescale of cooling (Kring et al., 2020).

Few studies have directly constrained the crystallization history of large impact melt sheets but high-precision U–Pb geochronology of zircon offers such a possibility. Davis (2008) trialed an experimental high-precision geochronological technique (thermal extraction–thermal ionization mass spectrometry; TE–TIMS) on newly grown zircon from two samples from the approximately 2.5 km-thick Sudbury impact melt sheet (Ontario, Canada), and suggested that crystallization of the body took hundreds of kyr. However, the Paleoproterozoic age of the Sudbury structure means that even the uncertainties offered by high-precision geochronology cannot easily parse the timescales of impact melt crystallization suggested by thermal modeling (e.g., Abramov and Kring, 2004, 2007). Being relatively young and large, Chicxulub offers the best target for high-precision zircon U–Pb geochronology. However, the main body of the melt sheet is buried under approximately 1 km of post-impact sediments (Kring, 1995) and has not yet been extensively drilled or sampled. Conversely, the impact melt sheet at Morokweng has been intersected by a number of drill holes, including the >1000 m M3 borehole which intersects ~800 m of impact melt rock. At *ca*. 145 Ma (Hart et al., 1997; Koeberl et al., 1997), the melt sheet at Morokweng currently offers the theoretically highest absolute precision on individual grains and samples of any known terrestrial impact structure.

The Morokweng impact structure in northwest South Africa (Fig. 1a) is almost entirely covered by Cenozoic Kalahari Group sediments. As such, most impact-related evidence comes from drill holes which have penetrated the structure (Fig. 1b), with size constraints largely based on regional geophysical data. Estimates for the diameter of the Morokweng impact structure have varied significantly. For example, on discovery of the structure, Corner et al. (1997; p. 351) suggested that its original size was likely "at least 70 km" but circular features in geophysical data "could be interpreted as indicating a diameter of 300-340 km", and Andreoli et al. (1999) have suggested a diameter of approximately 260 km, based on arcuate outcrops of Archean cover rocks and surface drainage trends. A consensus has yet to be reached but the observation of limited deformation in the KHK-1 borehole (Fig. 1a) appears to constrain the maximum present-day diameter to about 75-80 km (Reimold et al., 2002). A diameter in this approximate range would also be consistent with initial interpretations that the M4 borehole, approximately 18 km from the center of the structure (Fig. 1a), appears to have intersected the peak ring (Gibson et al., 2019). The diverse target rocks at Morokweng, known from boreholes and scattered outcrops, include Archean and Proterozoic granitoids, metavolcanics, metasediments, ultramafics, banded iron formations, as well as Phanerozoic sediments and intrusive and extrusive mafic rocks (e.g., Andreoli et al., 1999; Corner et al., 1997; Koeberl and Reimold, 2003; Reimold et al., 2002). A number of boreholes at Morokweng have intersected igneous rocks representing a crystallized body of impact melt (Fig. 1b). The impact melt sheet is unconformably overlain by Kalahari Group sedimentary rocks in each of the boreholes, i.e. an unknown thickness of impact melt rock and overlying breccias has been eroded away. The deepest borehole into the melt sheet, M3, intersected approximately 80 m of calcrete, sandstone, and pebbly mudstone before passing through ~800 m of impact melt rocks and ~170 m of shocked and brecciated amphibolite gneisses and subsidiary leucogranite that are interpreted as crater basement. The impact melt rocks in M3 can be divided into three sections: (i) the lowermost melt rock (from the contact with the footwall at ~872 m to ~847 m) that is distinctly microcrystalline with highly elongate and skeletal orthopyroxene needles and sheaf-like clusters of elongate plagioclase feldspar – this is interpreted as a chill zone at the base of the melt sheet; (ii) an overlying clast-laden granophyre (from ~847 m to ~700 m) that is generally fine grained but displays local heterogeneities in grain size and also contains meteorite fragments (Maier et al., 2006); and (iii) a relatively coarse-grained body that grades from norite to granophyric norite to granophyre (from ~700 m to the unconformity at ~80 m) as it transitions from relatively dark and mafic at its base to lighter and felsic at its top (Fig. 1b). Contacts between the units appear gradational and are complicated by the internal complexity of the melt sheet that could be related to a combination of assimilation of clasts, chill effects adjacent to large clasts, fluid-rich melt patches (particularly around amphibolite clasts), and late-stage mobilization of fluid-rich melt – see, for example, Andreoli et al. (1999) and Koeberl and Reimold (2003) for details of the complexity of impact melt rocks at Morokweng.

An absolute age for the Morokweng impact event has been established from minerals that crystallized from the impact melt. Isotope-dilution thermal ionization mass spectrometry (ID-TIMS) and secondary ion mass spectrometry (SIMS) analyses of zircon gave weighted mean $^{206}Pb/^{238}U$ dates of 145.2 ± 0.8 Ma (all uncertainties are shown at 2σ; Hart et al., 1997) and 146.2 ± 1.5 Ma (Koeberl et al., 1997), respectively. An $^{40}Ar/^{39}Ar$ weighted mean plateau age of 143.5 ± 3.6 Ma for biotite (Hart et al., 1997) is indistinguishable from the zircon U–Pb date. Here we aim to build on this work by providing the first high-precision U–Pb zircon age for the Morokweng impact structure in the era of chemical abrasion-isotope dilution-thermal ionization mass spectrometry (CA-ID-TIMS) (Mattinson, 2005) and the EARTHTIME initiative (Condon et al., 2015), enabling us to compare the most precise age for the structure with modern age constraints on the J–K boundary.

2. Materials and methods

2.1. Samples

Six samples from throughout the M3 borehole were selected for zircon U–Pb geochronology. The core samples were taken at the following depths: 117.5 m (M3-1), 401.1 m (M3-2), 611.1 m (M3-3), 700.6 m (M3-4), 700.8 m (M3-5), and 765.7 m (M3-6). Five of the samples, M3-1 to M3-5, were taken from the main body of impact melt rock and sample M3-6 was taken from the fine-grained, clast-laden granophyre beneath (Fig. 1b). McDonald et al. (2001) reported major and trace element whole rock data for samples above a depth of 480 m in the M3 borehole. We report data for additional samples above 480 m as well as data for 23 samples

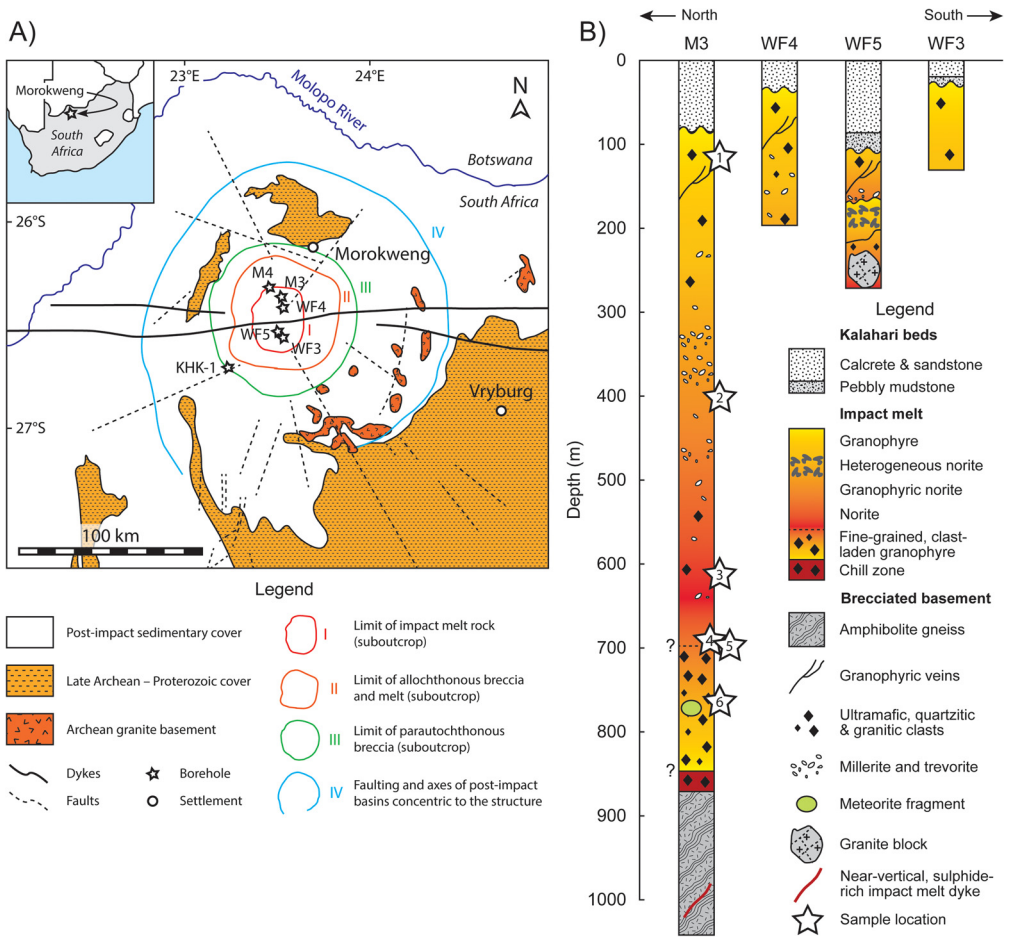

Fig. 1. Simplified geological map of the Morokweng impact structure, South Africa, and simplified stratigraphy of boreholes into the impact melt sheet. Modified after Andreoli et al. (1999) and Hart et al. (2002). Question marks refer to uncertainty in the nature of these contacts (see text). (For interpretation of the colors in the figures, the reader is referred to the web version of this article.)

from below 480 m to provide a full dataset for the approximately 800 m of preserved impact melt rock (Fig. 2). The whole rock data were used in MELTS modeling discussed below. Zircon was identified in thin section in five of the six samples from which it was separated (it was not identified in thin section in M3-2) and occurs alongside rock-forming minerals, predominantly quartz, alkali and plagioclase feldspar, and orthopyroxene (Supplementary Fig. 1).

2.2. Methods

A detailed description of the methods can be found in the supplementary appendix.

Whole rock major and trace element analysis. We analyzed 51 whole rock samples from the M3 borehole, which brings the number of data points presented to 63 when analyses from McDonald et al. (2001) are included. Lithophile major, minor, and trace element abundances were determined by X-ray fluorescence (XRF) at Lakefield Research Labs, Ontario, Canada. A range of trace elements (including REE) were measured in nine samples by ICP-MS at Genalysis, Perth, Australia. Whole rock data are presented in Supplementary Table 1 and data on standards and duplicates are presented in Supplementary Table 2.

MELTS modeling. We performed forward geochemical modeling using rhyolite-MELTS v1.02 (Gualda et al., 2012) to estimate the liquidus, zircon saturation, and solidus temperatures for an average composition of the Morokweng impact melt sheet (estimated from whole rock data from the M3 borehole; Supplementary Table 1).

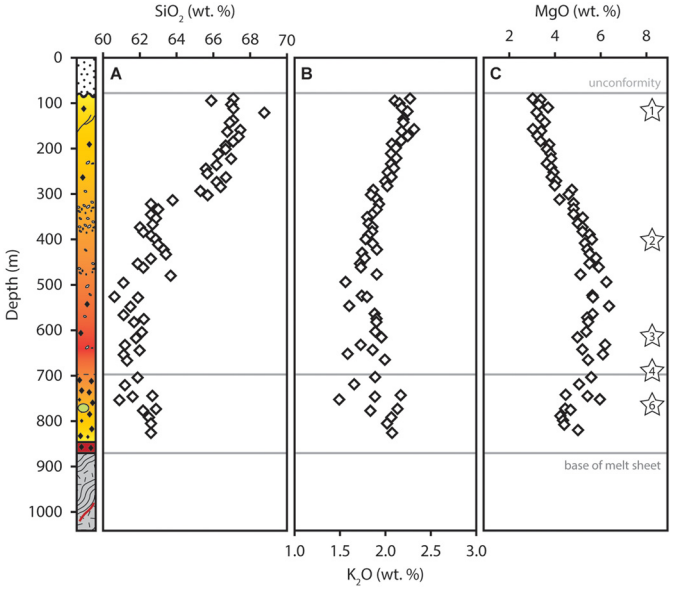

Fig. 2. Selected whole rock major element data for the M3 borehole. Twelve samples above 480 m are from McDonald et al. (2001) and the remaining data are from this study. Stars on right-hand side mark location of samples analyzed for high-precision geochronology.

The MELTS run was carried out at 18 MPa pressure in fractional crystallization mode at 5 °C temperature increments, starting from just above the liquidus down to 725 °C, at which point no melt remained. Further details are provided in the supplementary appendix.

Zircon chemistry and geochronology. The zircon separation process comprised crushing, milling, the use of a wet shaking table, and magnetic and heavy liquid density separation. High optical quality zircon grains were picked and annealed at 900 °C for 60 hours before being mounted in epoxy. The grains were then polished until their centers were exposed. After cathodoluminescence (CL) and backscattered electron (BSE) imaging (images of all analyzed zircon grains are available in Supplementary Figs. 2-7) the grains were analyzed for U–Pb isotopic data and trace element concentrations by *in situ* laser ablation-inductively coupled plasma mass spectrometry (LA-ICPMS). A selection of grains from five of the six samples were then plucked from the grain mount and underwent high-precision U–Pb analysis by CA-ID-TIMS. Samples M3-4 and M3-5 are from almost adjacent sections of the drill core so only M3-4 underwent high-precision analysis. Results of the LA-ICPMS analyses are reported in Supplementary Table 3 and details of the analytical setup and analyses of standard zircon are reported in Supplementary Tables 4 and 5. Results of the CA-ID-TIMS analyses are reported in Supplementary Table 6.

Baddeleyite U–Pb geochronology by ID-TIMS. Baddeleyite was identified in the heavy mineral separates of three of the samples (M3-1, M3-2, and M3-6). The protocol for baddeleyite U–Pb geochronology by ID-TIMS largely followed that used for zircon with the notable exceptions that baddeleyite was neither annealed nor chemically abraded.

Thermal modeling. We built a two-dimensional finite difference model of conductive cooling of the Morokweng impact melt sheet in the R software environment. Full details of the model and parameters used are presented in the supplementary appendix. The model is purely conductive, i.e. does not incorporate convective cooling associated with an impact-related hydrothermal system. Abramov and Kring (2007) demonstrated that the presence or absence of a hydrothermal system will not greatly affect the timescales of impact melt sheet cooling and crystallization because the melt sheet is impermeable while crystallizing and conduction is the dominant mechanism of heat transport. The air above the structure causes downward conductive cooling of the melt sheet (which is complemented by convective cooling via hydrothermal circulation of fluid in breccias overlying the melt sheet if such a system is present). We simulated these heat sinks by imposing a constant temperature (25 °C) upper boundary condition at the top of the model.

Impact melt is initially superheated, with crystallographic evidence from the 28-km-diameter Mistastin Lake impact structure, Canada, showing that impact melts can reach temperatures >2370 °C (Timms et al., 2017). However, the effective initial temperature of an impact melt sheet may be significantly lower than this as heat is transferred into clasts incorporated into the melt (e.g., Onorato et al., 1978). Consequently, a number of thermal models for the cooling of impact melts used conservative initial temperatures of 1700 °C (e.g., Abramov and Kring, 2004, 2007). We ran our model with an initial melt sheet temperature of 2370 °C to provide a maximum constraint on the duration of melt sheet cooling. We also ran the model with an initial melt sheet temperature of 1700 °C for comparison with the higher temperature model run and to allow direct comparison with other models which used the more conservative value. A list of input parameters for the thermal model is given in Supplementary Table 7.

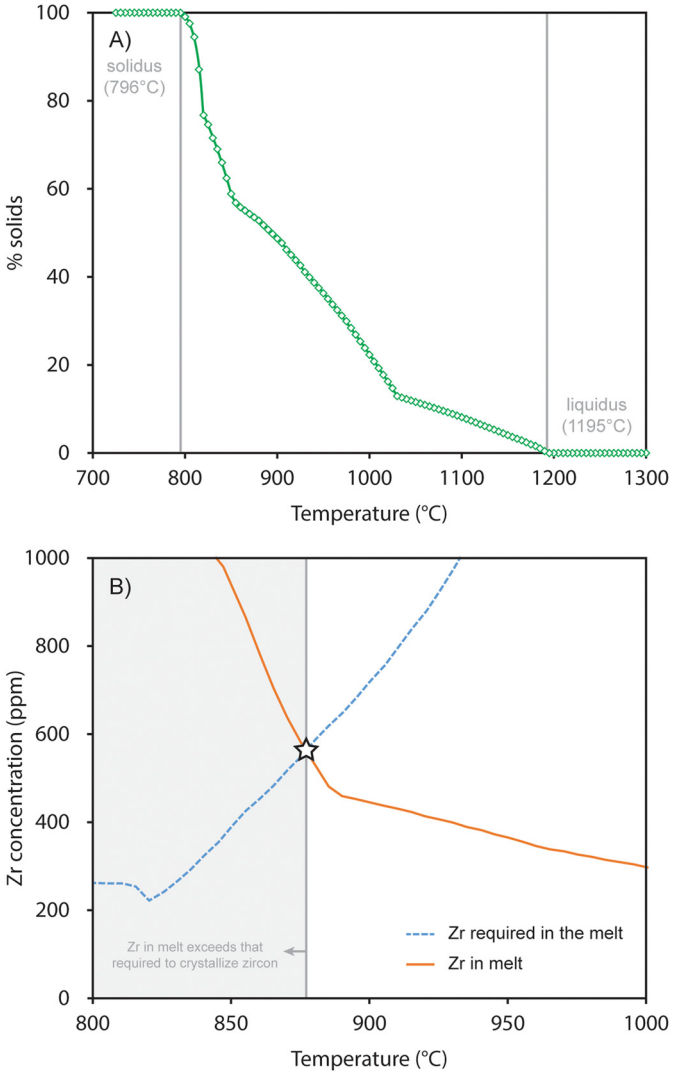

Fig. 3. Results of MELTS modeling for an average composition of the Morokweng impact melt sheet. a) Percentage of solids versus temperature, used to define the liquidus and solidus temperatures. b) Evolution of Zr concentration in the melt with decreasing temperature during crystallization. On cooling to approximately 880 °C, the amount of Zr in the melt is sufficient for zircon to begin crystallizing, in agreement with Ti-in-zircon thermometry (Fig. 4).

3. Results

3.1. Whole rock major and trace element data

The main body of impact melt rock sampled by the M3 borehole at Morokweng is increasingly mafic with depth. SiO_2 decreases from ~67 wt.% towards the top of the preserved melt sheet (where zircon sample M3-1 was taken) to ~62 wt.% near the base of the main body (where M3-3 and M3-4 were sampled), with K_2O also decreasing from ~2.25 wt.% to ~1.75 wt.% and MgO increasing from ~3 wt.% to ~6 wt.% (Fig. 2). However, the trend does not continue into the clast-laden basal unit. The whole rock composition of the basal unit (~63 wt.% SiO_2, ~2.0 wt.% K_2O, and ~4.5 wt.% MgO) is more felsic than the immediately overlying material in the unit above (Fig. 2).

3.2. MELTS modeling

The results of the MELTS modeling for an average composition of the Morokweng impact melt sheet at the M3 borehole are shown in Fig. 3. The MELTS modeling indicates a liquidus temper-

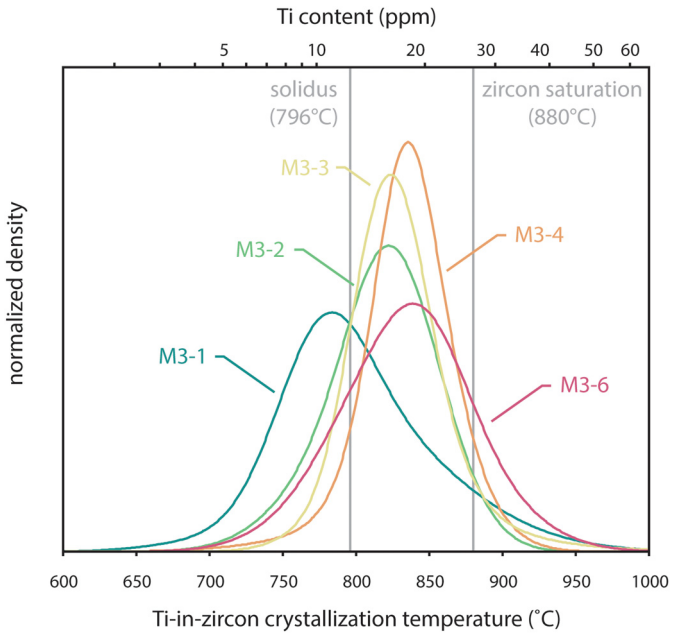

Fig. 4. Kernel density estimates (KDEs) of Ti-in-zircon crystallization temperatures for samples from the M3 borehole analyzed for high-precision geochronology. Two analyses that gave Ti concentrations >40 ppm (both in sample M3-6) were excluded on the assumption that they represent excess Ti associated with crystal imperfections. Conversion from Ti content to Ti-in-zircon crystallization temperature utilized the calibration of Ferry and Watson (2007), assuming αTiO_2 of 0.75 and αSiO_2 of 1. Solidus and zircon saturation temperatures obtained from MELTS modeling of an average composition of the Morokweng impact melt sheet.

ature of 1195 °C and that zircon saturation can be achieved using the proposed parental melt as a starting composition – consistent with the presence of zircon. The concentration of Zr, an incompatible element, in the melt increases during crystallization of the major cumulus minerals (i.e. Zr-free minerals) and zircon saturation occurs with just over 45% remaining residual melt at temperatures ranging from 880 °C down to 860 °C, depending on the Zr concentration chosen for initial conditions. These temperatures are directly comparable with those determined by Ti-in-zircon thermometry (Fig. 4). Crystallization is complete by 796 °C, which is considered the approximate solidus temperature of the melt sheet.

3.3. Zircon geochemistry

The concentration of Ti in zircon is dependent on crystallization temperature and thus can be integrated with liquidus, zircon saturation, and solidus temperatures to offer insight into the significance of high-precision zircon dates in the context of a crystallizing magma (Ferry and Watson, 2007; Watson et al., 2006). The six samples studied for zircon geochemistry have mean concentrations of Ti in zircon ($\pm 1\sigma$) varying between 19 ± 9 ppm (n = 29; excluding two outliers of 46 and 132 ppm) in the stratigraphically lowest sample, M3-6, and 14 ± 6 ppm (n = 15) in the stratigraphically highest sample, M3-1 (Fig. 4; Supplementary Table 3). The data agree with the values that Wielicki et al. (2012) reported for two samples from the same borehole. Using the calibration of Ferry and Watson (2007) and assuming αTiO_2 of 0.75 and αSiO_2 of 1, the new samples have mean Ti-in-zircon crystallization temperatures varying between 839 ± 42 °C (M3-6) and 801 ± 44 °C (M3-1). The Ti-in-zircon crystallization temperatures generally lie between the approximate temperature at which zircon became saturated in the melt, 880 °C, and the solidus temperature, 796 °C (Fig. 4), producing a consistent model for zircon saturation and crystallization within the solidifying impact melt. That a minority of zircon analyses (n = 29 of 169) have Ti-in-zircon crystallization temperatures below the solidus temperature (Fig. 4) could be a result of variations in the factors controlling the calibration of the Ti-in-zircon thermometer, or could reflect the fact that the solidus value for an average melt sheet composition approximates that of the system and cannot be valid for every location at which zircon was sampled.

3.4. High-precision U–Pb geochronology of zircon

In situ U–Pb geochronology by LA-ICPMS (conducted simultaneously with trace element analysis) indicates that all zircon grains analyzed in the six samples have dates of *ca*. 145 Ma (Supplementary Table 3). This agrees with previous estimates for the age of the Morokweng impact melt sheet (Hart et al., 1997; Koeberl et al., 1997) and indicates no inheritance of zircon from the target rocks – consistent with observations at other large impact melt sheets, such as at Sudbury, Canada (Darling et al., 2009; Kenny et al., 2016; and references therein). Up to ten zircon grains, or fragments thereof, from each of five samples were subsequently analyzed for high-precision age determination by CA-ID-TIMS. Almost all analyses within each sample cluster tightly and lie on the concordia curve within the bounds of decay constant uncertainties (Fig. 5; Supplementary Table 6). The single exception is one analysis from sample M3-1 that gave a slightly younger date; the younger date can be attributed to the presence of a minor domain that experienced Pb loss, despite chemical abrasion largely removing such areas of the grains. Weighted mean dates for the majority of samples have MSWD values of less than 1.5 and probabilities of fit greater than 0.05 (Fig. 6), indicating internally consistent data without excess scatter. Additionally, there are no systematic variations in Ti content, and associated Ti-in-zircon crystallization temperature, with high-precision $^{206}Pb/^{238}U$ dates within samples (Supplementary Fig. 8). This suggests that the selected crystals are representative of the sample and the use of weighted mean dates is appropriate. The four stratigraphically highest samples, from the main body of the Morokweng impact melt sheet (M3-1 to M3-4), have indistinguishable weighted mean dates (Fig. 6). Only the lowermost sample, M3-6, representing the fine-grained, clast-laden granophyre towards the base of the melt sheet (Fig. 1b), has a distinguishable relative date (Fig. 6). For the dates shown in Fig. 6, the uncertainties only include internal errors; this means that they are suitable for comparison with each other but generally not for comparison with dates using a different tracer or isotopic system. When additional uncertainties are considered, all five samples have uncertainties of ±0.05 Ma upon inclusion of the tracer calibration uncertainty and ±0.16 Ma upon inclusion of the ^{238}U decay constant uncertainty; for example, the stratigraphically highest sample, M3-1, has a date of 146.056 ± 0.018 (0.050) [0.16] Ma.

3.5. High-precision U–Pb geochronology of baddeleyite

Baddeleyite was identified in three samples: M3-1, M3-2, and M3-6. The co-occurrence of baddeleyite and zircon, which require silica-undersaturated and silica-saturated conditions respectively, in the same rock is not unusual and can result from, for example, (i) a melt transitioning from silica-undersaturated to silica-saturated conditions during crystallization, or (ii) heterogeneities within a rock sample where centimeter-scale domains may have different silica-saturation conditions.

We analyzed between three and five grains of baddeleyite per sample by ID-TIMS. The baddeleyite grains did not return consistent $^{206}Pb/^{238}U$ dates but gave dates that spread between 150 and 300 kyr younger than the zircon dates for the same sample (Fig. 5; Supplementary Table 6). The discrepancy between the dates obtained from zircon and those obtained from baddeleyite

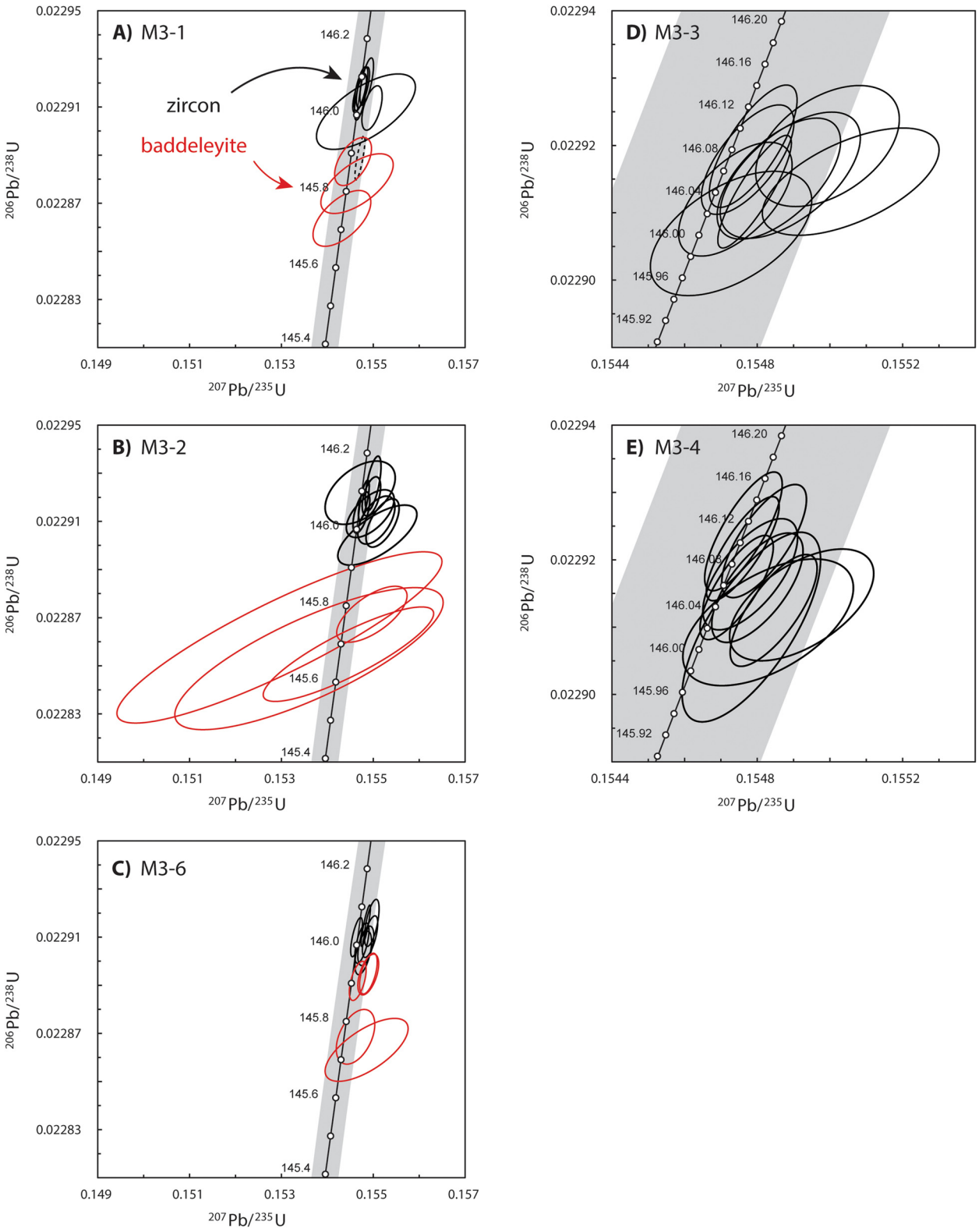

Fig. 5. Concordia diagrams showing CA-ID-TIMS U–Pb geochronological data. Black and red ellipses represent data from zircon and baddeleyite, respectively. All ellipses plotted at 2σ uncertainty. The younger date recorded by the dashed ellipse in (A) is likely due to minor post-impact Pb loss and, therefore, this analysis is not included in weighted mean calculations (Fig. 6). Grey shading represents decay constant uncertainties.

could be primary, i.e. baddeleyite crystallized hundreds of kyr after zircon, or secondary, i.e. zircon and baddeleyite crystallized at the same time (within analytical uncertainty) but the baddeleyite grains give younger dates due to variable amounts of Pb loss from these crystals at some point after they crystallized. The spread in baddeleyite dates within samples (in contrast to zircon which defined coherent populations; Fig. 5) and the fact that there is not yet a well-established routine for effectively removing domains of baddeleyite that have suffered later Pb loss (Rioux et al., 2010) lead us to attribute the younger baddeleyite dates to Pb loss. The

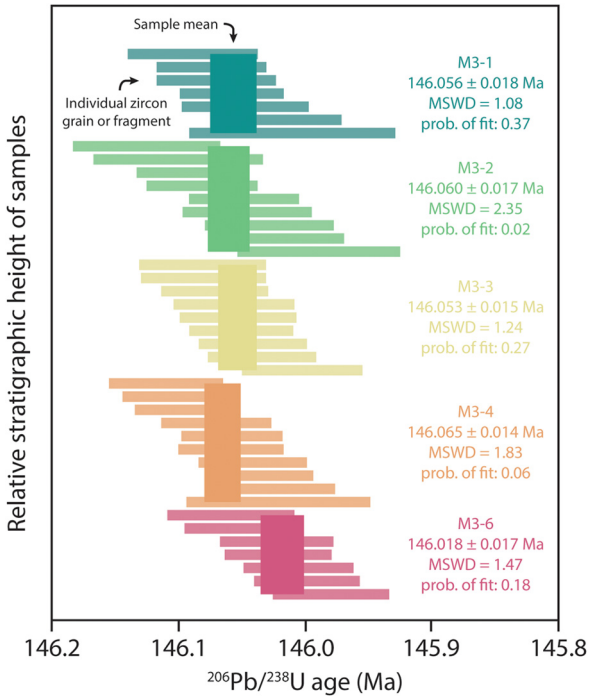

Fig. 6. Zircon CA-ID-TIMS U–Pb geochronological data. Samples ordered according to relative stratigraphic height (Fig. 2). One analysis from sample M3-1 is not included here as it appears to have experienced minor Pb loss (Fig. 5). MSWD – mean square of weighted deviates. Prob. – probability.

observed discrepancy between U–Pb dates for zircon and baddeleyite that crystallized in the relatively simple igneous system of an impact melt sheet cautions that baddeleyite dates may not accurately record crystallization of the host rock.

3.6. Thermal modeling

Thermal modeling suggests that the Morokweng melt sheet cooled and crystallized over tens of thousands of years, with the center of the melt sheet and underlying footwall rocks retaining heat, and thus melt-present conditions, for longer than the M3 borehole location (Figs. 7–8).

A one-dimensional profile at the M3 borehole shows rapid cooling from the initial temperature perturbation (Fig. 8a). The preserved portions of the melt sheet at the M3 borehole region solidified in less than 30 kyr (Fig. 8a), and the center of the melt sheet shows a similar pattern but with slightly elevated temperatures for a given time step (Fig. 8b). As a result of heat from the melt sheet transferring into the underlying crust, which was already elevated in temperature as a result of rapid uplift from depth at the time of impact, super-solidus temperatures in footwall rocks below the center of the melt sheet persist for tens of kyr after the melt sheet itself has reached the solidus. To quantify the length of time that melt was present in the system, and able to migrate within the structure, we calculated the time until a depth corresponding to twice the thickness of the melt sheet (an arbitrarily chosen value equating to 2.3 km below the surface) passed through the solidus. This is 65 kyr after impact.

We determined the relative timing of zircon crystallization by determining when each sample location passed through the zircon saturation (880 °C) and solidus (796 °C) temperatures. We plotted the temperature with depth at 0.1 kyr intervals and compared those paths with the sample depth and the zircon saturation and solidus temperatures (Supplementary Fig. 9). We interpret the model result of temperature with depth at 0.1 kyr intervals that most closely intersects the sample depth and temperature of interest as the zircon saturation age or solidification age (Supplementary Table 8). The model results can also be illustrated by the time-temperature paths of the nodes closest to each sample. Rapid cooling in the melt sheet region over the first ~10 kyr is followed by decelerating cooling with time (Fig. 9). Our model predicts that samples M3-1, M3-2, M3-3, M3-4, and M3-6 reached solidus temperatures 11.0, 18.0, 22.9, 24.9, and 26.4 kyr after impact, respectively.

We compare the weighted mean U–Pb zircon absolute dates to the thermal model relative ages in Fig. 10. The U–Pb zircon weighted mean dates and uncertainties of the upper four samples overlap with the thermal model prediction for zircon crystallization. Notably, the U–Pb zircon date of M3-6 is a few thousand years younger than the predicted thermal model zircon crystallization interval. While an adjustment to the anchoring of the two age-depth paths could force the thermal model to pass through the U–Pb zircon weighted mean date of M3-6, this adjustment would create a poor fit for the upper four samples. Therefore, we interpret the younger U–Pb zircon date of M3-6 as evidence that melt in the vicinity of this sample did not cool and crystallize by simple *in situ* conductive cooling like the melt sampled by the upper four samples. Further explanation is required to explain the younger date close to the base of the melt sheet.

We also ran the model with a much more conservative initial melt temperature of 1700 °C (Supplementary Figs. 10-11) that was used in a number of previous modeling studies (e.g., Abramov and Kring, 2004, 2007). In this scenario, the melt sheet is entirely solidified within ~25 kyr, i.e. just ~10 kyr faster than in the 2370 °C model. Melt-present conditions persist in footwall rocks beneath the melt sheet for ~55 kyr, i.e., ~10 kyr less than in the higher temperature model.

4. Discussion

4.1. Cooling and crystallization of the Morokweng melt sheet

Combined petrographic observations, MELTS modeling, Ti-in-zircon thermometry, high-precision U–Pb zircon geochronology, and thermal modeling provide a model for the cooling and crystallization of the Morokweng impact sheet as well as general insights into the timescales of impact melt crystallization at large impact structures.

After generation of a large body of well-mixed, superheated impact melt, the Morokweng impact melt sheet began to cool rapidly. At approximately 1200 °C, major cumulus phases began crystallizing from the melt. As crystallization proceeded, the concentration of Zr in the residual melt gradually increased and zircon saturation was reached at approximately 880 °C. Petrographic observations show that zircon crystallized contemporaneously with rock-forming minerals and Ti-in-zircon thermometry confirms that zircon crystallized over a range of temperatures between zircon saturation and complete solidification at approximately 796 °C (Fig. 4).

High-precision U–Pb geochronology of zircon from the M3 borehole at Morokweng directly dates crystallization in this approximately 880 to 796 °C window and can be compared with our thermal model to provide absolute constraints on impact melt crystallization. The modeled time interval over which the melt sheet cooled through zircon saturation and solidification agrees with the distribution of the U–Pb dates for the four upper most samples of impact melt rock (Fig. 10). This indicates that the model accurately describes the thermal evolution of the structure at this location and that much of the melt sheet sampled by the M3 borehole likely crystallized as a result of relatively simple top-down conductive cooling in less than 30 kyr. However, sample M3-6, from close to the base of the melt sheet in the M3 drill core, gives a zircon U–Pb date that is younger than that predicted by

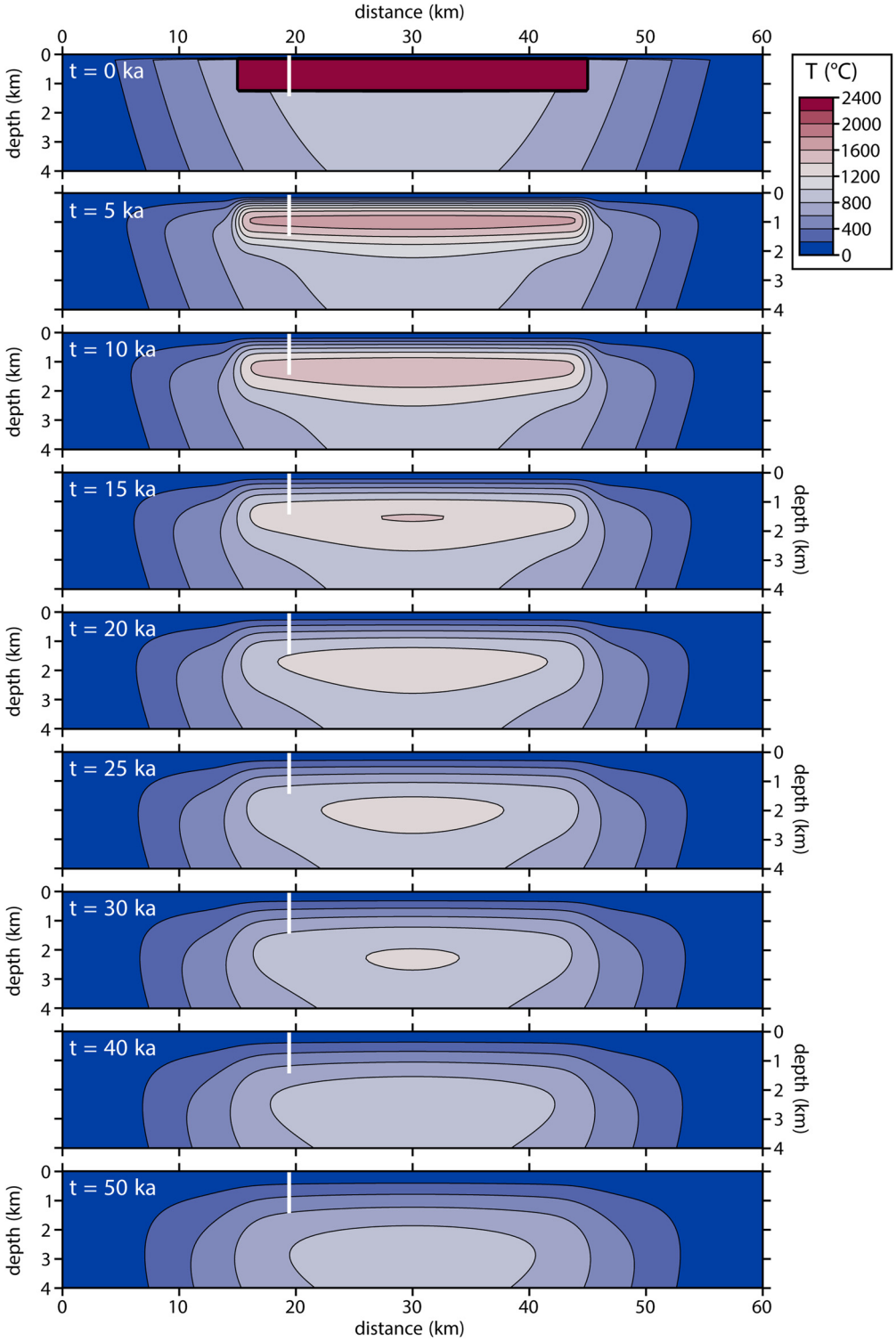

Fig. 7. Two-dimensional thermal model results with 200 °C isotherms. The uppermost panel illustrates the starting conditions of the model. The white line at x = 19.5 km indicates the location of the approximately 1 km-deep M3 borehole.

the model (Fig. 10), and therefore, requires an explanation other than top-down *in situ* conductive cooling.

The fine-grained, clast-laden granophyre beneath a depth of 700 m in the M3 borehole, from which sample M3-6 was taken, appears to be an *in situ* mixing zone where the superheated melt sheet intruded and assimilated the brecciated and shock-melted footwall basement, rock that was itself likely at temperatures >700 °C owing to uplift and shock heating. This model for the origin of this zone is consistent with its high clast content (Hart et al., 2002) and the observation that the basal unit is more felsic than the immediately overlying norite of the main body of melt (Fig. 2). Additionally, post-impact melting of footwall rocks is well documented at the Sudbury and Manicouagan impact structures, where melting of footwall rocks produced isotopic heterogeneities in what were initially well-mixed impact melts (Darling et al., 2010; O'Connell-Cooper et al., 2012). Consequently, we tested the

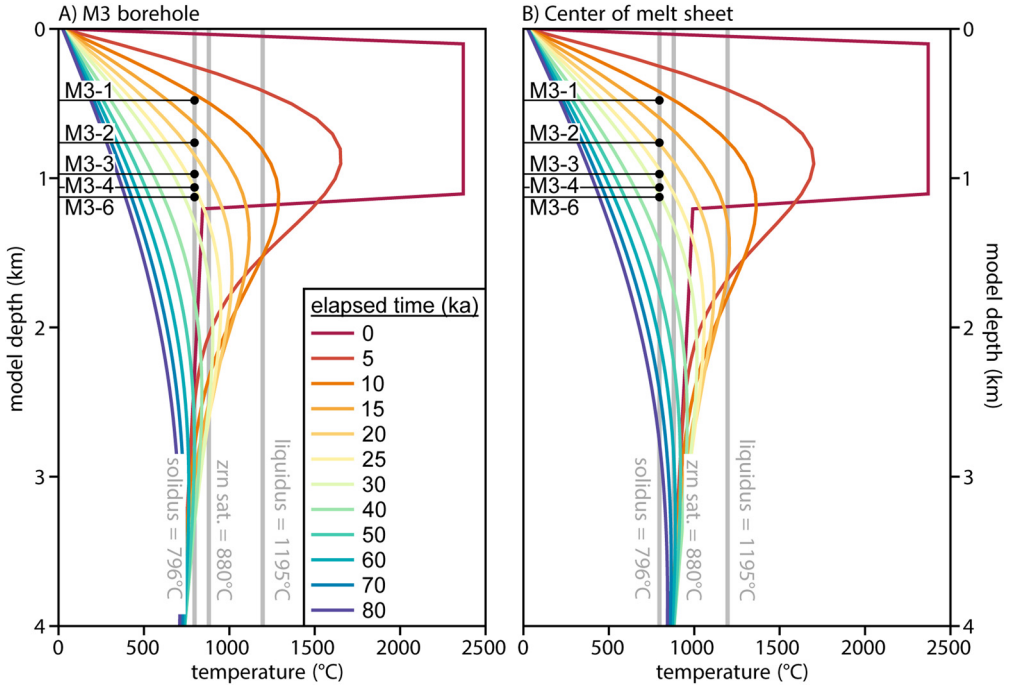

Fig. 8. One-dimensional temperature profiles with depth of (a) the M3 borehole (x = 19.5 km on Fig. 7) and (b) the geographic center of the melt sheet (x = 30 km on Fig. 7). The colored lines are interpolated results evaluated at nodes with depth spacing of 0.1 km. The legend in (a) also applies to (b). Sample depths are indicated by black dots on the solidus for reference. zrn sat. – zircon saturation temperature.

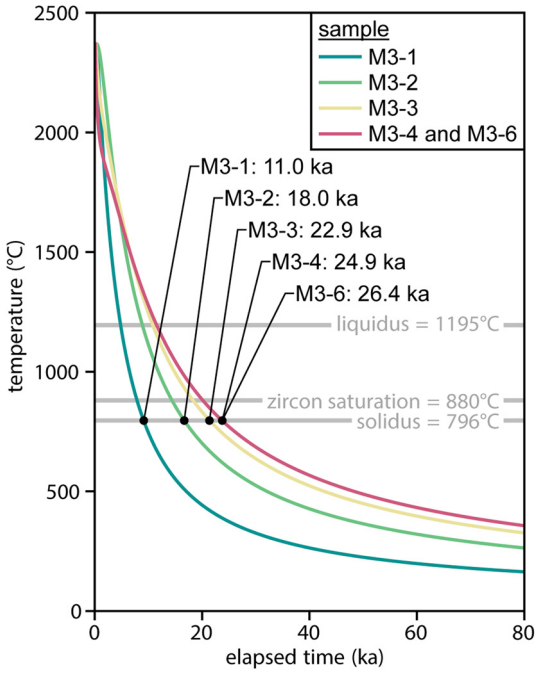

Fig. 9. Thermal model temperature-time path of M3 borehole samples. The time-temperature paths of samples M3-4 and M3-6 overlap because the similar depths of those samples cause them to be evaluated at the same node of the thermal model. Black dots indicate the intersection of the time-temperature path with the solidus temperature; see Supplementary Fig. 9 for details on determining the solidification ages.

hypothesis that local variations in the composition or water content of the fine-grained, clast-laden granophyre (resulting from, for example, dehydration and melting of footwall rocks or clasts entrained into the melt) is the reason for the younger U–Pb date of sample M3-6. By varying the melt composition to the most extreme values encountered in the melt sheet and water contents to a range of values between 0.1 and 3.0%, we were able to reduce the >10 kyr gap between modeled age and U–Pb date for M3-6 (Fig. 10) to ~5 kyr. However, no combination of composition and water content allowed the modeled age and U–Pb date to overlap. As such, the younger date of sample M3-6 cannot be explained by local variations in composition or water content alone.

A thermal profile through the center of the structure indicates that although the melt sheet sampled by the M3 borehole likely crystallized in less than 30 kyr, rock beneath the melt sheet was held at super-solidus conditions for ~65 kyr after impact (Fig. 8b). This leads to the question of whether melt could have migrated from beneath the center of the melt sheet to the area sampled by the M3 borehole late in the crystallization history of the system, resulting in the younger date for sample M3-6. Melt generation, accumulation, and migration has been documented beneath melt sheets at the largest terrestrial impact structures. At Sudbury, intrusions in the footwall and into the melt sheet have been attributed to accumulation and migration of partial melts from beneath the melt sheet (e.g., Jørgensen et al., 2018; Kenny et al., 2017; Péntek et al., 2011). At Vredefort, impact-aged granites have also been proposed as having an anatectic origin (Gibson et al., 1997; Gibson and Reimold, 2008). Despite these observations it is unlikely that a large volume of clast-rich melt could have migrated up to 10 km from the center of the melt sheet at Morokweng. However, there is some evidence to suggest that at least some of the fine-grained, clast-laden granophyre beneath 700 m in the M3 drill core is derived from elsewhere. For example, the clasts in the melt rock are mainly granitic, which is inconsistent with derivation from the predominantly amphibolite gneiss footwall immediately below. Furthermore, it is difficult to establish a detailed understanding of the melt sheet at this location from the single intersection offered by the M3 borehole. For example, although the fine-grained clast-laden granophyre at the base of the M3 borehole may be largely *in situ*, we cannot rule out that specimen M3-6 sampled a thin intersection of late melt sourced from beneath the melt sheet. In summary, (i) the zircon U–Pb dates for the upper four samples of the M3 borehole are consistent with top-down,

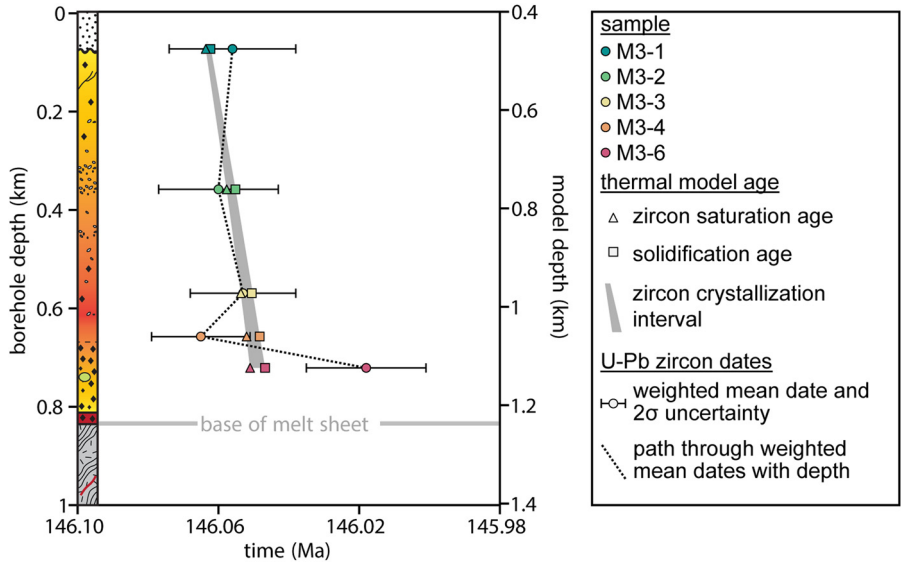

Fig. 10. Comparison of thermal model ages (zircon saturation age and solidification age) and U–Pb zircon dates. The borehole depth and stratigraphic section are on the left y-axis and the model depth, which assumes some erosion of the melt sheet, is on the right y-axis. The dashed line connects the weighted mean U–Pb zircon dates to illustrate the change in date with depth. The gray polygon connects the time-depth path of the zircon saturation and solidification ages, illustrating the range of time when zircon was crystallizing in these samples. The thermal model ages (which are relative ages) are anchored to the absolute U–Pb zircon dates by aligning the mean variance of the U–Pb weighted means and uncertainties of the upper four samples with the mean variance of the thermal model solidification ages of the same samples.

conductive cooling in less than 30 kyr, and (ii) the reason for the younger date of sample M3-6 remains uncertain but the date is within the ~65 kyr timeframe of melt-present conditions below the impact melt sheet indicated by our thermal model.

Modeling the Morokweng melt sheet with a much more conservative initial melt temperature indicates that an effective starting temperature of 1700 °C (instead of 2370 °C) would lead to crystallization of the melt sheet and termination of melt-present conditions in the footwall just ~10 kyr earlier. Therefore, a lower initial melt temperature (conceivably a result of heat transfer into clasts incorporated into the melt; Onorato et al., 1978) is also consistent with our geochronological results and proposed model for the younger age of sample M3-6. Finally, we note that the thermal perturbation caused by the impact persisted for over 2.5 Myr (Supplementary Fig. 12).

4.2. Scaling up the thermal model and application to Chicxulub – a young, large impact structure

As our thermal model offers an explanation for the high-precision geochronology results from the Morokweng impact melt sheet, we here scaled it up to investigate the cooling and crystallization of melt sheets at larger impact structures. To model the conductive cooling of a Chicxulub-sized (~180 km in diameter; Kring, 1995) impact structure, we adopted the parameters and approximate dimensions used by Abramov and Kring (2007). We ran the model twice – once with the initial temperature of the melt set to 1700 °C, as assumed by Abramov and Kring (2007), and a second time with the melt starting at 2370 °C.

A vertical one-dimensional temperature profile through the center of the Chicxulub-scale melt sheet indicates that if the melt started cooling from an initial temperature of 1700 °C it would have crystallized in ~100 kyr (Supplementary Fig. 13). This is in agreement with Abramov and Kring's (2007) model for purely conductive cooling of the Chicxulub structure (their Fig. 6), in which the melt sheet crystallized between the 20 and 200 kyr time steps. The results of our conductive cooling model for a Chicxulub-sized impact structure are also consistent with estimates for the crystallization of the melt sheet at the similarly-sized Sudbury impact structure. Purely conductive models for Sudbury indicated that melt sheet crystallization was complete by 97 kyr (Prevec and Cawthorn, 2002) or 130 kyr (Abramov and Kring, 2004) after impact.

There is abundant evidence for hydrothermal alteration at Chicxulub (e.g., Kring et al., 2020, and references therein) and, as such, Abramov and Kring (2007) incorporated into their model convective cooling associated with a large hydrothermal system. As noted above in reference to Morokweng, Abramov and Kring (2007) found that at Chicxulub conduction was the dominant mechanism of heat transport and that the hydrothermal system had a limited role on the cooling and crystallization of the main body of impact melt. As such, our purely conductive model likely approximates the timeframe of melt solidification well.

We also ran our Chicxulub-scale model with an initial melt temperature of 2370 °C to be consistent with the potential for higher initial melt temperatures, as suggested by Timms et al. (2017). In this scenario, the time it takes for the melt sheet to crystallize increases to ~150 kyr (Supplementary Fig. 13). As such, we suggest that the conservative initial melt temperature of 1700 °C assumed by Abramov and Kring (2007) may be a reason that their model might be "too conservative and underestimates the lifetime of the system", as indicated by hydrothermal mineral assemblages in the structure's peak ring (Kring et al., 2020; p. 6). Consequently, we propose that effective initial impact melt temperatures, even after cooling due to heat transfer to incorporated clasts is taken into consideration (Onorato et al., 1978), are likely closer to 2370 °C than the commonly assumed value of 1700 °C.

We estimated the length of time that melt-present conditions persisted in the footwall rocks after the overlying melt sheet had crystallized in a similar manner as done at Morokweng – by interpreting super-solidus conditions as temperatures above 800 °C (an estimated solidus temperature for footwall rocks) within a depth corresponding to twice the thickness of the melt sheet (i.e. within 6 km of the surface at Chicxulub). We found that melt was present beneath the Chicxulub melt sheet for ~300 kyr after the melt sheet had solidified (Supplementary Fig. 13).

The 66 Ma age of Chicxulub means that it offers an unrivaled opportunity to constrain the timescales of impact structure cooling with high-precision U–Pb geochronology and complementary thermal modeling. Therefore, we propose that drilling of the central melt sheet of the Chicxulub impact structure should be a high priority for the geoscience community.

4.3. Age of the Morokweng impact event and its relation to the Jurassic–Cretaceous boundary

The impact melt sheet at Morokweng cooled from the top downwards (Figs. 7–8) and, as such, the stratigraphically highest sample will have crystallized first and be closest in age to the impact event. The thermal model indicates that the stratigraphically highest sample, M3-1, solidified 11.0 kyr after the impact event (Fig. 9). Thus, the impact event occurred within uncertainty of the high-precision U–Pb date from sample M3-1: 146.06 ± 0.16 Ma (2σ; full external uncertainty), and we can interpret this date as the age of the impact event. The new age is within uncertainty of previous absolute ages for the Morokweng event (Hart et al., 1997; Koeberl et al., 1997) but approximately an order of magnitude more precise.

Since the establishment of a *ca*. 145 Ma age for the Morokweng impact event (Hart et al., 1997; Koeberl et al., 1997), it has been noted that this coincides with the ∼145 Ma absolute age of the J–K boundary, as it was then, and is now, formally recognized (e.g., by the International Commission on Stratigraphy; Cohen et al., 2013 updated). However, when Morokweng was first dated, uncertainty regarding the nature of extinction events around the J–K boundary and difficulties establishing the exact stratigraphic position of the boundary (and therefore its absolute age) precluded any conclusion that the impact may have played a role in a J–K boundary extinction event (Hart et al., 1997; Koeberl et al., 1997).

The J–K boundary was once considered one of eight mass extinctions events in the past 250 Myr (e.g., Raup and Sepkoski, 1986) but this view has largely been overturned, and the intensity, timing, and geographic extent of any putative extinction event, or events, around or across the J–K boundary remain debated (e.g., Tennant et al., 2017, and references therein). Additionally, there is still no officially recognized position of the stratigraphic boundary, i.e. Global Boundary Stratotype Section and Point (GSSP), for the J–K boundary. However, there is growing evidence that the absolute age of the J–K boundary, at least at some locations, is closer to 140 Ma than the *ca*. 145 Ma age traditionally proposed. High-precision U–Pb geochronology of tuffs in western Tethys (proto-Gulf of Mexico) and Andean basins constrains the J–K boundary in this region to ∼140 Ma (e.g., Vennari et al., 2014) or even 140.7–140.9 Ma (Lena et al., 2019), and the boundary is set to 143.1 ± 0.6 Ma in the Geological Time Scale 2020 (Gradstein et al., 2020) on the basis of magnetostratigraphy and cycle scaling (Gale et al., 2020). Consequently, the 146 Ma Morokweng impact preceded the J–K boundary by several million years, and evidence for the impact and any potential effects on the biosphere might be found in late Jurassic (Tithonian) successions.

5. Conclusions

High-precision U–Pb geochronology was performed on five samples from the impact melt sheet at the ∼80-km-diameter Morokweng impact structure, South Africa. Cast within in a framework of petrographic observations, MELTS thermodynamic modeling, Ti-in-zircon thermometry, and conductive thermal modeling, indistinguishable dates for four of the samples are consistent with full melt sheet crystallization within ∼35 kyr of the impact. A younger date from the stratigraphically lowest sample cannot be explained by *in situ* conductive cooling in line with the overlying samples but the date is within the ∼65 kyr timeframe for melt-present conditions below the impact melt sheet indicated by our thermal model.

Scaling up our thermal model indicates that the melt sheet at a Chicxulub-scale structure would crystallize within 100 to 150 kyr of the impact event. Being relatively young and large, Chicxulub offers an unrivaled opportunity to constrain the timescales of cooling of large impact structures with high-precision U–Pb geochronology of zircon.

The Morokweng impact is here constrained to 146.06 ± 0.16 Ma (2σ; full external uncertainty). Given recent work suggesting that the J–K boundary is likely younger than 143.1 ± 0.6 Ma (Gradstein et al., 2020), the 146 Ma Morokweng impact preceded the J–K boundary by several million years and any potential effects on the biosphere could be found in late Jurassic successions.

CRediT authorship contribution statement

Gavin G. Kenny: Conceptualization, Funding acquisition, Investigation, Methodology, Visualization, Writing – original draft, Writing – review & editing. **Claire O. Harrigan:** Investigation, Methodology, Software, Visualization, Writing – original draft, Writing – review & editing. **Mark D. Schmitz:** Funding acquisition, Supervision, Writing – review & editing. **James L. Crowley:** Supervision, Writing – review & editing. **Corey J. Wall:** Investigation, Writing – review & editing. **Marco A.G. Andreoli:** Resources, Writing – review & editing. **Roger L. Gibson:** Resources, Writing – review & editing. **Wolfgang D. Maier:** Investigation, Writing – review & editing.

Declaration of competing interest

The authors declare that they have no known competing financial interests or personal relationships that could have appeared to influence the work reported in this paper.

Acknowledgements

Kenny acknowledges a Fulbright Scholarship sponsored by the Geological Survey of Ireland, which facilitated his stay at the Isotope Geology Laboratory at Boise State University. This project also received funding from the European Union's Horizon 2020 research and innovation program under the Marie Skłodowska-Curie Individual Fellowship Grant Agreement No. 792030 to Kenny. Funding for the analytical infrastructure of the Boise State University Isotope Geology Laboratory was provided by the National Science Foundation (NSF) Major Research Instrumentation grants EAR-0521221 and EAR-1337887, and NSF EAR Instrumentation and Facilities Program grant EAR-0824974. We thank Darin Schwartz, Debbie Pierce, Kate Grosswiler, and Mike Mohr at the Isotope Geology Laboratory for support in the collection and interpretation of this data, and we thank the management of the South African Nuclear Energy Corporation for access to the M3 borehole core. Finally, we thank Christian Koeberl for a helpful review and Bill McKinnon for editorial handling.

Appendix A. Supplementary material

Supplementary material related to this article can be found online at https://doi.org/10.1016/j.epsl.2021.117013.

References

Abramov, O., Kring, D.A., 2004. Numerical modeling of an impact-induced hydrothermal system at the Sudbury crater. J. Geophys. Res., Planets 109, E10007. https://doi.org/10.1029/2003JE002213.

Abramov, O., Kring, D.A., 2007. Numerical modeling of impact-induced hydrothermal activity at the Chicxulub crater. Meteorit. Planet. Sci. 42, 93–112. https://doi.org/10.1111/j.1945-5100.2007.tb00220.x.

Abramov, O., Mojzsis, S.J., 2009. Microbial habitability of the Hadean Earth during the late heavy bombardment. Nature 459, 419–422. https://doi.org/10.1038/nature08015.

Andreoli, M.A.G., Ashwal, L.D., Hart, R.J., Huizenga, J.M., 1999. Petrology and geochemistry of nickel and iridium-rich quartz norite from the late Jurassic Morokweng impact structure, South Africa. In: Dressler, B.O., Sharpton, V.L. (Eds.), Large Meteorite Impacts and Planetary Evolution II. In: Geol. Soc. Am. Spec. Publ., vol. 339, pp. 91–108.

Cohen, K.M., Finney, S.C., Gibbard, P.L., Fan, J.-X., 2013. The ICS international chronostratigraphic chart. Updated (v 2020/03). Episodes 36, 199–204. https://doi.org/10.18814/epiiugs/2013/v36i3/002.

Condon, D.J., Schoene, B., McLean, N.M., Bowring, S.A., Parrish, R.R., 2015. Metrology and traceability of U–Pb isotope dilution geochronology (EARTHTIME Tracer Calibration Part I). Geochim. Cosmochim. Acta 164, 464–480. https://doi.org/10.1016/j.gca.2015.05.026.

Corner, B., Reimold, W.U., Brandt, D., Koeberl, C., 1997. Morokweng impact structure, Northwest Province, South Africa: geophysical imaging and shock petrographic studies. Earth Planet. Sci. Lett. 146, 351–364. https://doi.org/10.1016/S0012-821X(96)00210-5.

Darling, J.R., Hawkesworth, C.J., Lightfoot, P.C., Storey, C.D., Tremblay, E., 2010. Isotopic heterogeneity in the Sudbury impact melt sheet. Earth Planet. Sci. Lett. 289, 347–356. https://doi.org/10.1016/j.epsl.2009.11.023.

Darling, J.R., Storey, C.D., Hawkesworth, C.J., 2009. Impact melt sheet zircons and their implications for the Hadean crust. Geology 37, 927–930. https://doi.org/10.1130/g30251a.1.

Davis, D.W., 2008. Sub-million-year age resolution of Precambrian igneous events by thermal extraction-thermal ionization mass spectrometer Pb dating of zircon: application to crystallization of the Sudbury impact melt sheet. Geology 36, 383–386. https://doi.org/10.1130/g24502a.1.

Ferry, J.M., Watson, E.B., 2007. New thermodynamic models and revised calibrations for the Ti-in-zircon and Zr-in-rutile thermometers. Contrib. Mineral. Petrol. 154, 429–437. https://doi.org/10.1007/s00410-007-0201-0.

Gale, A.S., Mutterlose, J., Batenburg, S., Gradstein, F.M., Agterberg, F.P., Ogg, J.G., Petrizzo, M.R., 2020. The Cretaceous period. In: Gradstein, F.M., Ogg, J.G., Schmitz, M.D., Ogg, G.M. (Eds.), Geologic Time Scale 2020. Elsevier, Amsterdam, pp. 1023–1086.

Gibson, R.L., Armstrong, R.A., Reimold, W.U., 1997. The age and thermal evolution of the Vredefort impact structure: a single-grain U-Pb zircon study. Geochim. Cosmochim. Acta 61, 1531–1540. https://doi.org/10.1016/S0016-7037(97)00013-6.

Gibson, R.L., Reimold, W.U., 2008. Geology of the Vredefort impact structure: a guide to sites of interest (vol. 97). In: South African Council for Geoscience, Memoir 97. 181 pp.

Gibson, R.L., Wela, S.S., Andreoli, M.A.G., 2019. Structural analysis of the M4 drill core, Morokweng impact structure (South Africa) – implications for peak ring formation processes. In: Large Meteorite Impacts and Planetary Evolution Conference VI. Abstract #5051.

Gradstein, F.M., Ogg, J.G., Schmitz, M.D., Ogg, G.M., 2020. Geologic Time Scale 2020. Elsevier, Amsterdam.

Gualda, G.A.R., Ghiorso, M.S., Lemons, R.V., Carley, T.L., 2012. Rhyolite-MELTS: a modified calibration of MELTS optimized for silica-rich, fluid-bearing magmatic systems. J. Petrol. 53, 875–890. https://doi.org/10.1093/petrology/egr080.

Hart, R.J., Andreoli, M.A.G., Tredoux, M., Moser, D., Ashwal, L.D., Eide, E.A., Webb, S.J., Brandt, D., 1997. Late Jurassic age for the Morokweng impact structure, southern Africa. Earth Planet. Sci. Lett. 147, 25–35. https://doi.org/10.1016/S0012-821X(97)00006-X.

Hart, R.J., Cloete, M., McDonald, I., Carlson, R.W., Andreoli, M.A.G., 2002. Siderophile-rich inclusions from the Morokweng impact melt sheet, South Africa: possible fragments of a chondritic meteorite. Earth Planet. Sci. Lett. 198, 49–62. https://doi.org/10.1016/S0012-821X(02)00497-1.

Ivanov, B.A., 2004. Heating of the lithosphere during meteorite cratering. Sol. Syst. Res. 38, 266–279. https://doi.org/10.1023/B:SOLS.0000037462.56729.ba.

Ivanov, B.A., 2005. Numerical modeling of the largest terrestrial meteorite craters. Sol. Syst. Res. 39, 381–409. https://doi.org/10.1007/s11208-005-0051-0.

Jørgensen, T.R.C., Tinkham, D.K., Lesher, C.M., Petrus, J.A., 2018. Decoupling of Zr-Hf during contact metamorphic anatexis of metabasalts and timing of zircon growth, Sudbury, Canada. Geology 46, 159–162. https://doi.org/10.1130/G39590.1.

Kenny, G.G., Petrus, J.A., Whitehouse, M.J., Daly, J.S., Kamber, B.S., 2017. Hf isotope evidence for effective impact melt homogenisation at the Sudbury impact crater, Ontario, Canada. Geochim. Cosmochim. Acta 215, 317–336. https://doi.org/10.1016/j.gca.2017.08.009.

Kenny, G.G., Whitehouse, M.J., Kamber, B.S., 2016. Differentiated impact melt sheets may be a potential source of Hadean detrital zircon. Geology 44, 435–438. https://doi.org/10.1130/G37898.1.

Koeberl, C., Armstrong, R.A., Reimold, W.U., 1997. Morokweng, South Africa: a large impact structure of Jurassic-Cretaceous boundary age. Geology 25, 731–734. https://doi.org/10.1130/0091-7613(1997)025<0731:msaali>2.3.co;2.

Koeberl, C., Reimold, W.U., 2003. Geochemistry and petrography of impact breccias and target rocks from the 145 Ma Morokweng impact structure, South Africa. Geochim. Cosmochim. Acta 67, 1837–1862. https://doi.org/10.1016/S0016-7037(02)00994-8.

Kring, D.A., 1995. The dimensions of the Chicxulub impact crater and impact melt sheet. J. Geophys. Res. 100, 16979. https://doi.org/10.1029/95JE01768.

Kring, D.A., Tikoo, S.M., Schmieder, M., Riller, U., Rebolledo-Vieyra, M., Simpson, S.L., Osinski, G.R., Gattacceca, J., Wittmann, A., Verhagen, C.M., Cockell, C.S., Coolen, M.J.L., Longstaffe, F.J., Gulick, S.P.S., Morgan, J.V., Bralower, T.J., Chenot, E., Christeson, G.L., Claeys, P., Ferrière, L., Gebhardt, C., Goto, K., Green, S.L., Jones, H., Lofi, J., Lowery, C.M., Ocampo-Torres, R., Perez-Cruz, L., Pickersgill, A.E., Poelchau, M.H., Rae, A.S.P., Rasmussen, C., Sato, H., Smit, J., Tomioka, N., Urrutia-Fucugauchi, J., Whalen, M.T., Xiao, L., Yamaguchi, K.E., 2020. Probing the hydrothermal system of the Chicxulub impact crater. Sci. Adv. 6. https://doi.org/10.1126/sciadv.aaz3053.

Lena, L., López-Martínez, R., Lescano, M., Aguire-Urreta, B., Concheyro, A., Vennari, V., Naipauer, M., Samankassou, E., Pimentel, M., Ramos, V.A., Schaltegger, U., 2019. High-precision U–Pb ages in the early Tithonian to early Berriasian and implications for the numerical age of the Jurassic–Cretaceous boundary. Solid Earth 10, 1–14. https://doi.org/10.5194/se-10-1-2019.

Maier, W.D., Andreoli, M.A.G., McDonald, I., Higgins, M.D., Boyce, A.J., Shukolyukov, A., Lugmair, G.W., Ashwal, L.D., Gräser, P., Ripley, E.M., Hart, R.J., 2006. Discovery of a 25-cm asteroid clast in the giant Morokweng impact crater, South Africa. Nature 441, 203–206. https://doi.org/10.1038/nature04751.

Marchi, S., Bottke, W.F., Elkins-Tanton, L.T., Bierhaus, M., Wuennemann, K., Morbidelli, A., Kring, D.A., 2014. Widespread mixing and burial of Earth's Hadean crust by asteroid impacts. Nature 511, 578–582. https://doi.org/10.1038/nature13539.

Mattinson, J.M., 2005. Zircon U–Pb chemical abrasion ("CA-TIMS") method: combined annealing and multi-step partial dissolution analysis for improved precision and accuracy of zircon ages. Chem. Geol. 220, 47–66. https://doi.org/10.1016/j.chemgeo.2005.03.011.

McDonald, I., Andreoli, M.A.G., Hart, R.J., Tredoux, M., 2001. Platinum-group elements in the Morokweng impact structure, South Africa: evidence for the impact of a large ordinary chondrite projectile at the Jurassic-Cretaceous boundary. Geochim. Cosmochim. Acta 65, 299–309. https://doi.org/10.1016/S0016-7037(00)00527-5.

O'Connell-Cooper, C.D., Dickin, A.P., Spray, J.G., 2012. The Manicouagan impact melt sheet: evidence for isotopic homogenization with limited assimilation. Earth Planet. Sci. Lett. 335–336, 48–58. https://doi.org/10.1016/j.epsl.2012.04.033.

Onorato, P.I.K., Uhlmann, D.R., Simonds, C.H., 1978. The thermal history of the Manicouagan impact melt sheet, Quebec. J. Geophys. Res., Solid Earth 83, 2789–2798. https://doi.org/10.1029/JB083iB06p02789.

Osinski, G.R., Cockell, C.S., Pontefract, A., Sapers, H.M., 2020. The role of meteorite impacts in the origin of life. Astrobiology 20. https://doi.org/10.1089/ast.2019.2203.

Péntek, A., Molnár, F., Watkinson, D.H., Jones, P.C., Mogessie, A., 2011. Partial melting and melt segregation in footwall units within the contact aureole of the Sudbury Igneous Complex (North and East Ranges, Sudbury structure), with implications for their relationship to footwall Cu–Ni–PGE mineralization. Int. Geol. Rev. 53, 291–325. https://doi.org/10.1080/00206810903101313.

Prevec, S.A., Cawthorn, R.G., 2002. Thermal evolution and interaction between impact melt sheet and footwall: a genetic model for the contact sublayer of the Sudbury Igneous Complex, Canada. J. Geophys. Res. 107. https://doi.org/10.1029/2001JB000525.

Raup, D.M., Sepkoski, J.J., 1986. Periodic extinction of families and genera. Science 231, 833–836. https://doi.org/10.1126/science.11542060.

Reimold, W.U., Armstrong, R.A., Koeberl, C., 2002. A deep drillcore from the Morokweng impact structure, South Africa: petrography, geochemistry, and constraints on the crater size. Earth Planet. Sci. Lett. 201, 221–232. https://doi.org/10.1016/S0012-821X(02)00658-1.

Rioux, M., Bowring, S., Dudás, F., Hanson, R., 2010. Characterizing the U–Pb systematics of baddeleyite through chemical abrasion: application of multi-step digestion methods to baddeleyite geochronology. Contrib. Mineral. Petrol. 160, 777–801. https://doi.org/10.1007/s00410-010-0507-1.

Schulte, P., Alegret, L., Arenillas, I., Arz, J.A., Barton, P.J., Bown, P.R., Bralower, T.J., Christeson, G.L., Claeys, P., Cockell, C.S., Collins, G.S., Deutsch, A., Goldin, T.J., Goto, K., Grajales-Nishimura, J.M., Grieve, R.A.F., Gulick, S.P.S., Johnson, K.R., Kiessling, W., Koeberl, C., Kring, D.A., MacLeod, K.G., Matsui, T., Melosh, J., Montanari, A., Morgan, J.V., Neal, C.R., Nichols, D.J., Norris, R.D., Pierazzo, E., Ravizza, G., Rebolledo-Vieyra, M., Reimold, W.U., Robin, E., Salge, T., Speijer, R.P., Sweet, A.R., Urrutia-Fucugauchi, J., Vajda, V., Whalen, M.T., Willumsen, P.S., 2010. The Chicxulub asteroid impact and mass extinction at the Cretaceous-Paleogene boundary. Science 327, 1214–1218. https://doi.org/10.1126/science.1177265.

Tennant, J.P., Mannion, P.D., Upchurch, P., Sutton, M.D., Price, G.D., 2017. Biotic and environmental dynamics through the Late Jurassic–Early Cretaceous transition: evidence for protracted faunal and ecological turnover. Biol. Rev. 92, 776–814. https://doi.org/10.1111/brv.12255.

Timms, N., Erickson, T., Zanetti, M., Pearce, M., Cayron, C., Cavosie, A., Reddy, S., Wittmann, A., Carpenter, P., 2017. Cubic zirconia in >2370 °C impact melt

records Earth's hottest crust. Earth Planet. Sci. Lett. 477, 52–58. https://doi.org/10.1016/j.epsl.2017.08.012.

Vennari, V.V., Lescano, M., Naipauer, M., Aguirre-Urreta, B., Concheyro, A., Schaltegger, U., Armstrong, R., Pimentel, M., Ramos, V.A., 2014. New constraints on the Jurassic–Cretaceous boundary in the High Andes using high-precision U–Pb data. Gondwana Res. 26, 374–385. https://doi.org/10.1016/j.gr.2013.07.005.

Wielicki, M.M., Harrison, T.M., Schmitt, A.K., 2012. Geochemical signatures and magmatic stability of terrestrial impact produced zircon. Earth Planet. Sci. Lett. 321, 20–31. https://doi.org/10.1016/j.epsl.2012.01.009.

Watson, E.B., Wark, D.A., Thomas, J.B., 2006. Crystallization thermometers for zircon and rutile. Contrib. Mineral. Petrol. 151, 413. https://doi.org/10.1007/s00410-006-0068-5.